
Article:
Garum, M orcid.org/0000-0002-4703-4350, Glover, PWJ orcid.org/0000-0003-1715-5474, Lorinczi, P et al. (2 more authors) (2021) Integration of Multiscale Imaging of Nanoscale Pore Microstructures in Gas Shales. Energy and Fuels, 35 (13). pp. 10721-10732. ISSN 0887-0624

https://doi.org/10.1021/acs.energyfuels.1c00554

Integration of Multi-Scale Imaging of Nanoscale Pore Microstructures in Gas Shales

Mohamed Garum[1], Paul W.J. Glover[2], Piroska Lorinczi[2], Stuart Micklethwaite[1], Ali Hassanpour*[1]
[1]School of Chemical and Process Engineering, University of Leeds, Leeds LS2 9JT, U.K.
[2]School of Earth and Environment, University of Leeds, Leeds LS2 9JT, U.K.
*Corresponding author (A.H): Tel: +44(0)113 343 2405; Email: A.Hassanpour@leeds.ac.uk

Abstract
Quantification of the microstructures of shales is difficult due to their complexity which extends across many orders of magnitude of scale. Nevertheless, shale microstructures are extremely important, not only as shale gas resources, but as cap-rocks in CCS resources, in geothermal reservoirs and as a host to the long-term storage of radioactive materials. In this work, we have carried out ultra-high resolution CT imaging (nano-CT), mercury injection porosimetry (MIP) and nitrogen adsorption experiments on a sample of gas shale for which we already have focussed ion beam scanning electron microscopy (FIB-SEM) and high resolution CT (micro-CT) datasets. The combination of these datasets has allowed us to examine the microstructure of the shale in unprecedented depth across a wide range of scales (from about 20 nm to 0.5 mm). Overall the sample shows a porosity of 0.67±0.009% from the nano-CT data, 0.0235±0.003% from nitrogen adsorption, and 0.60±0.07% from MIP, which compare with 0.10±0.01%, 0.52±0.05%, 0.94±0.09% from 3 FIB-SEM measurements and 0.06±0.008% from one micro-CT measurements The data vary due to the different scales at which each technique interrogates the rock and whether the pores are openly accessible (especially in the case of the nitrogen adsorption value). Measured kerogen fraction is 32.4±1.45% from nano-CT, compared with 34.8±1.74%, 38.2±1.91%, 41.4±2.07%, and 44.5±2.22% for 3 FIB-SEM and one micro-CT measurement. The pore size imaged by nano-CT ranged between 100 nm to 5000 nm, while the corresponding ranges were between 3 and 2000 nm for MIP analysis and between 2 nm to 90 nm for N_2 adsorption. The distribution of pore aspect ratio and scale-invariant pore surface area to volume ratio (σ) as well as the calculated permeability shows the sample to have a high shale gas potential. Aspect ratios indicate that most of the pores which contribute significantly to pore volume are oblate, which is confirmed by the range of σ (3 to 13). Oblate pores have greater potential for interacting with other pores compared to equant and needle-shaped prolate pores, as well optimising surface area for gas to desorb from the kerogen into the pores. Permeability essays provide 2.61±0.42 nD from the nano-CT data, 2.65±0.45 nD from MIP, and (5.07±0.02) $\times 10^{-4}$ nD from nitrogen adsorption, which are consistent with expectations for generic gas shales (i.e., tens of nD) and the measurements made previously on the same sample using FIB-SEM and micro-CT imaging techniques.

Keywords. Permeability, Porosity, Kerogen, pore volume, pore size distribution, pore aspect ratio and surface area to pore volume, Gas shale, Nano-CT, MIP and nitrogen adsorption (N_2)

1. Introduction

The internal microstructure and nanostructure of shale rocks provides valuable information for understanding the quality of the shale gas reservoir as well as the efficacy of shale cap-rocks [1]. Important microstructural parameters include pore size and volume distributions, the distributions of pore aspect ratios, the distributions of surface area to volume ratios, as well as overall porosity and tensor permeability [2]. However, obtaining accurate measurement of these properties remains a major challenge, partly because shales are extremely complex, but also because their microstructure is controlled by extremely small scale pores [3]. In consequence, shale porosities commonly vary between 2% and 15 % [4, 5], but always have extremely small permeabilities, typically below < 10^{-18} m^2 [6].

Accurate characterisation of shale gas resource not only depends on the overall porosity and permeability of the shales but also on the microstructural and nanostructural properties of the shale, because it is these properties that control the location and amount of hydrocarbon storage but also the connectivity of hydrocarbon flow paths [7]. Interactions between the rock matrix and the fluids it contains have also to be taken into account. Wettability is the measurement of the affinity of the fluid surface to the different fluids in the rock pores, which depends on both the mobile and static fluids in the rock as well the rock's microstructure and nanostructure [8].

Previous studies have used a number of petrophysical methods to investigate the microstructural properties of shale rocks samples [4, 9, 10], including low pressure nitrogen adsorption and the mercury injection (capillary) pressure (MIP) methodolgies. The MIP technique is commonly used on shales and measures the incremental volume of mercury that enters the rock in response to incrementally increasing applied mercury pressure [11]. This technique is used to measure pore throat sizes extremely successfully in high porosity clastic and carbonate rocks (5 μm-500 μm), but can also measure pore throat sizes in range 2-5000 nm, with sufficiently high injection pressures [12]. However, the MIP method is regarded as unsuitable for use on gas shales [13]. Shales have extremely small pore sizes. The high mercury pressures that are required to push mercury into even the largest of the shale pores are large enough to compress the shale rock sample and consequently compress the pores or lead to sample breakage. The results obtained might provide smaller pore size distributions than expected from compression, or the presence of larger spaces that result from sample deformation and breakage [14]. Another disadvantage of the MIP technique is that the sample must be dried before use. Such a desiccation process has little effect on the microstructure of clean sands and carbonates, but causes large and irreversible changes to the internal structure of shales [14].

Low pressure nitrogen adsorption is suitable for measurements of the small pores that typify shales (2 nm up to 300 nm) [10], and is also capable of providing information on the shape of pores, which is important in understanding the controls on the accessibility of hydrocarbon. However, this method also requires drying and evacuation of samples (in order to remove the volatiles from the shale samples such as chemical elements, N_2, CO_2) before the test.

Hence, in principle, both of these measurements are able to detect pore sizes in the range 2 to 300 nm in shales, but the results need to be interpreted with caution [15]. In this work they are interpreted with reference to ultra-high resolution 3D X-Ray tomography measurements. The comparison between the three measurement approaches allows the precision of each technique to be examined.

Numerous imaging techniques have also been used for visualising and quantifying shale samples in three dimensions (3D). These techniques include, X-ray Computed Tomography at various scales (e.g., conventional low resolution CT, micro-CT, nano-CT, [16, 17]), Focused Ion Beam Scanning Electron Microscopy (FIB-SEM) [18, 19], and Transmission Electron Microscopy (TEM) tomography [4]. The main purpose of the 3D imaging characterizations is usually to understand the type of the pores, their geometry, size, volume, surface area and the connectivity of the pores, as well as the relationships between pores and minerals.

In shale materials however, the matrix has unconnected porosity due to complex pore structure and highly heterogeneous nature, thus, the microstructure and pore systems cannot be described at a single scale [16]. Therefore, multi-scale imaging techniques are required to characterize the shale microstructure.

This paper extends our previous work [17] by using the same sample volume to characterize the 3D microstructure using the nano-CT method in order to bridge the gap in information between previously obtained FIB-SEM data, which has a maximum pore size and volume resolution of about 20 nm and 0.008 μm^3, respectively, and micro-CT, which has a minimum pore size and volume resolution of about 930 nm and 0.804 μm^3, again respectively [17]. We then compare the combined multi-CT dataset with allied measurements made using the MIP and nitrogen absorption techniques to (i) examine the extent to which each measurement provides a consistent description of the nanostructure and microstructure of the shale, and (ii) to arrive at a full multi-scale quantitative characterisation of the complex pore system and microstructure of Bowland gas reservoir shales.

The quantification and multi-scale measurements presented in this study can be useful in areas other than gas shales, such as in nuclear waste disposal [20], geothermal reservoir development [21], and the construction of fuel cells [22].

2. Material and methods

2.1 Sample material and preparation

The shale gas sample was collected from a 2700 m depth from the Bowland shale formation which is located in the North West of England, UK (the same sample as used in [17]).

A very small cuboid sample (side length about 25 µm) was prepared from the reservoir rocks by using FIB-SEM system as a manipulation and preparation tool. The preparation procedures have already been published, and are given in [23].

2.2 X-Ray Diffraction

An X-ray diffraction (Bruker D8 XRD) measurement was performed to determine the mineralogical phases present within shale samples (Table 1). These measurements were carried out in the School of Chemical and Process Engineering at the University of Leeds and have an error of approximately ± 1%.

2.3 Nitrogen gas adsorption measurements

The nitrogen (N_2) gas adsorption measurements were made on the same sample using a Micromeritics Tristar 3000 instrument in the School of Chemical and Process Engineering at the University of Leeds. This procedure provided information on porosity and pore size, internal surface area, pore volume, as well as pore and surface area to pore volume distributions. The shale samples were crushed into powder with particle sizes < 250 μm before measurement.

The pore volume and pore sizes were determined using the Barrett Joyner-Halenda (BJH) method [24], while the pore surface areas were obtained by using the Brunauer-Emmett-Teller (BET) theory [25].

2.4 Mercury injection capillary pressure measurements

The Mercury injection (MIP) measurements were made using a Micromeritics Autopore IV 9520 system in the School of Earth and Environment, University of Leeds. The measurement was carried out on a chip sample of around 2 mm size with a weight of around 10 g. It should be noted that the measured chip was that from which the 3D imaging samples had been prepared. The shale chip sample was evacuated under a pressure of 70 μm Hg for approximately 15 min before the test. A mercury filling pressure of 0.51 psi was applied for 10 s for equilibration, and was then followed by the injection of mercury at high pressure, starting from 1.9 psi up to the maximum 60,000 psi in logarithmically incrementing. The starting pressure corresponds to a largest measureable pore-throat diameters of 3 μm, while the high ultimate pressure corresponds to the smallest pore that can be measured at 90.7 nm. The MIP data was inverted using standard techniques to obtain the pore throat distribution of the sample as well as its total porosity.

2.5 Multi-scale 2D/3D imaging techniques

Three methods were used to visualise and quantify the 3D microstructure of a sample of Bowland gas shale. The methods are (i) Focused Ion Beam Scanning Electron Microscopy (FIB-SEM), (ii) nano-scale X-ray computed tomography (nano-CT), and (iii) micron-scale X-ray computed tomography (micro-CT). Taken together, the three measurement methods allow length scales from 10^{-3} m to 10^{-9} m to be imaged and quantified.

It is important to note that all three measurements were made on exactly the same sample of shale such that the measurements are directly comparable. The whole sample

(approximately 500×500×1000 μm) was imaged using the micro-CT technique, while the nano-CT and FIB-SEM techniques were applied to regions of this sample as shown in Figure 1. The micro-CT and FIB-SEM data have already been presented in our previous work [17], where information may be found on the instruments, voxel resolution and field of view.
In this study, we perform and present the nano-CT measurements and the supporting MIP and nitrogen adsorption data. The nano-CT data was measured using a ZEISS Ultra Nano-CT instrument at the University of Manchester (as outlined in [23]). Measurements were made on a cuboid sample (Figure 2b) with a side length of approximately 25 μm and a voxel size of approximately 64x64x64 nm^3 .

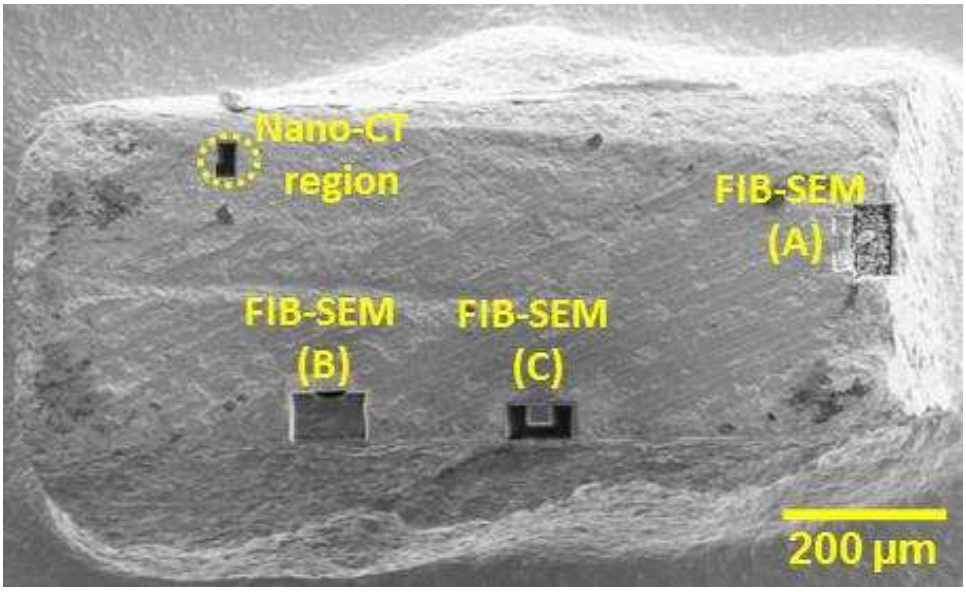

Figure 1. An overview of the Bowland gas shale sample used in this study, showing the location of the nano-CT measurements (top left) and the three different positions (A, B, and C) that were used for FIB-SEM serial sectioning.

Multi-scale image acquisition was undertaken using three different imaging techniques (micro-CT, nano-CT and FIB-SEM), providing the 2D and 3D microstructure of the shale sample to be visualised over 6 orders of magnitude in length scale. At the largest scales, imaged using the micro-CT technique, the voxel resolution is approximately 1 μm (930x930x930 nm^3). Consequently, only pores greater than 1 μm (and extending to 1000 μm) can be visualised. At this scale the pores are apparently unconnected (Figure 2a). There may be (and as we shall see later in this paper is) connectivity between the pores, but those connections are in the form of pathways that are too small to be visualised by the micro-CT technique (i.e., are smaller than 1 μm) [17].

At a smaller scale, around 100 nm, the nano-CT technique still has difficulty resolving connectivity between the pores (Figure 2b) because its voxel size (64x64x64 nm^3) is insufficient. However, the nano-CT is able to resolve connectivity for the kerogen, as can be seen in Figure 3e.

The FIB-SEM technique has the smallest resolution (voxel size of 19x24x20 nm^3) is able to reveal more details of the microstructure such as pores, kerogen and matrix. The small fractures that provide connections between the larger pores can be recognized at this higher resolution (Figure 2c), but some of the larger pores which are thus connected are too large to be imaged. Indeed, the cost of this technique having such a good resolution is that it can only image a small volume of rock (17 µm×17 µm×30 µm) which makes the technique unable to visualise the phenomena larger than about 5 µm. The pervasive connections at the ultra-small scale measured by FIB-SEM provide the pathways for flow that give gas shales their small, but non-zero, permeability of several to several thousand nanodarcies).

Pores with a diameter lower than about 20 nm cannot be detected using any of the techniques used in this work.

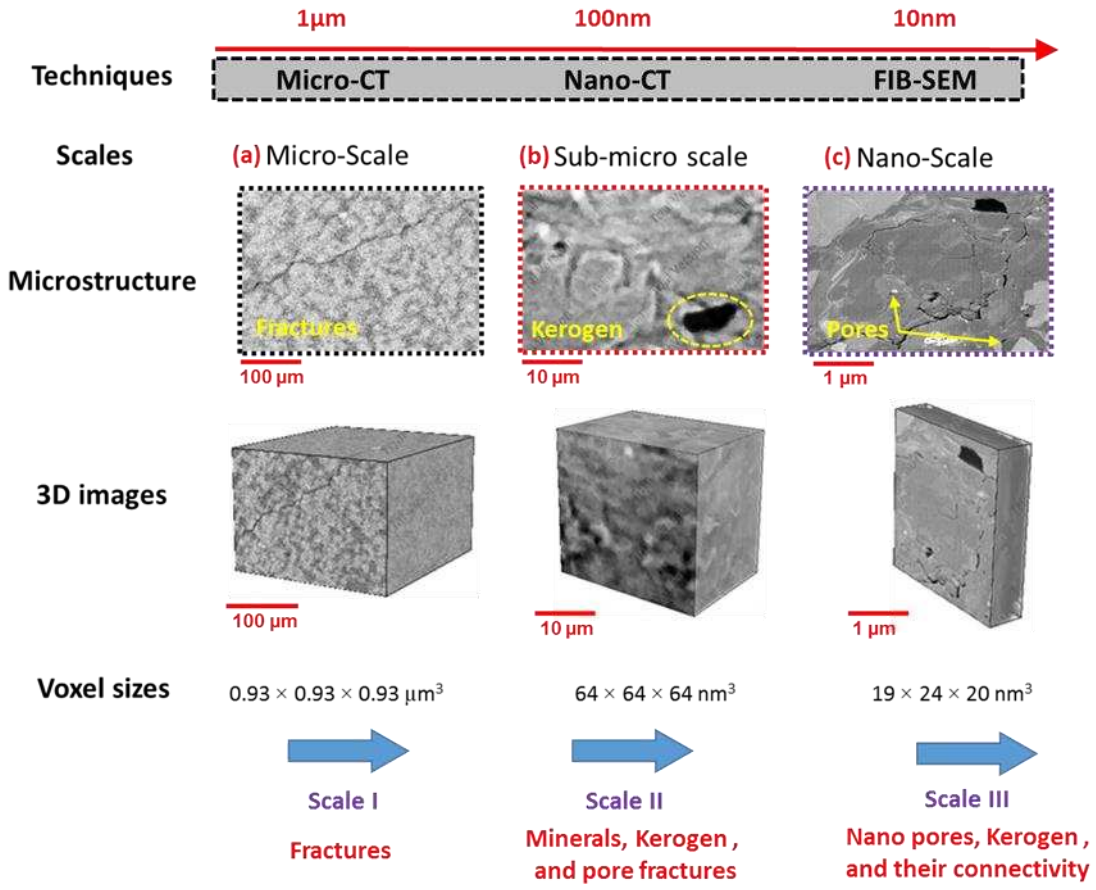

Figure 2. Multi-scale imaging of the FIB-SEM, nano-CT and micro-CT techniques applied in this study on the same volume of shale rock sample.

2.6 2D/3D Imaging analysis

The data from all 2D/3D imaging techniques were analysed using a protocol of image processing techniques such as filtering, thresholding, segmentation and quantification [17, 23]. This process was carried out using Avizo®9.0 software and resulted in a wide range of numerical measurements including pore size, pore volume, pore surface area, and pore dimensions, for each recognised pore. These initial data were used to calculate distributions of pore number, volume, aspect ratios, scale invariant surface area to volume ratio as a function of scale (i.e., pore size). Further details of the methodologies used can be found in [17, 19, 23].

3. Results

3.1 Mineral composition analysis and kerogen fraction

Standard XRD analysis was used to identify the mineralogical composition of the shale sample (Table 1). The sample contains predominantly quartz, mica and dolomite together with a smaller amount of pyrite, with proportions of 92.5 vol%, 4.6 vol%, 1.4 vol% and 0.7 vol%, respectively.

Despite kerogen representing an important fraction of shales, both volumetrically and with regard to its significance as a resource, it is not possible to calculate from XRD measurements. Nevertheless, the results of XRD analysis can provide valuable adjunct information for understanding the mineralogy composition and phases in shale samples [26]. In this paper, we have used 3D image analysis of the nano-CT data to obtain the volumetric fraction of the kerogen phase fraction as 32.4±1.45 vol%.

Table 1. Volume percentage fraction of major minerals from XRD measurements.

Sample	Quartz	Albite	Microcline	Dolomite	Mica	Siderite	Pyrite
MD-2.7 Km (vol%)	92.5	0.6	0.2	1.4	4.6	0.1	0.7

3.2 3D Microstructure of Gas Shale Volumes

The 3D micro-structure of the shale sample has been investigated using Nano-CT images of slices/sections through the sample (Figure 3).

Figure 3 shows the three-dimensional images of the sample acquired using Nano-CT with significant parameters related to gas transport such as pore, kerogen, and matrix phase fractions. Figure 3a shows the raw 3D grey-scale image of the sample on its support needle and from another aspect. This data volume has been thresholded to separate pores, kerogen and the rock matrix. The remainder of the figure assigns the red colour to kerogen, blue to pores and green to rock matrix. Figures 3b shows all three different phases. The remaining

parts of the figure show single phases and combinations of two phases, the last of which shows the pores colour-coded according to whether they are connected to each other. It can be seen that kerogen composes 32.4 vol% of the sample and is distributed anisotropically, with the kerogen predominantly represented by long thin bodies that are arranged sub-parallel. Qualitatively it appears that there is high connectivity between these kerogen bodies across large proportions of the whole 64×64×64 nm^3 sample volume (Figure 3e). By contrast, pores make up only 0.67±0.009 vol % of the sample (Figure 3f). Qualitatively, the pores are smaller, more numerous, more equant and apparently less connected. Figure 3g shows a 3D image of the pore space network where the colours indicate those pores which are connected. Apart from a couple of local patches, pores exist predominantly as apparently isolated entities, at least at the scale measured by the nano-CT technique. The FIB-SEM measurements [17] show that the apparent lack of connection of these pores is misleading. The volume fraction of the sample that was classed as matrix amounted to 66.93 vol%. Table 2 displays a brief summary of the most important data including pores and kerogen obtained by different techniques.

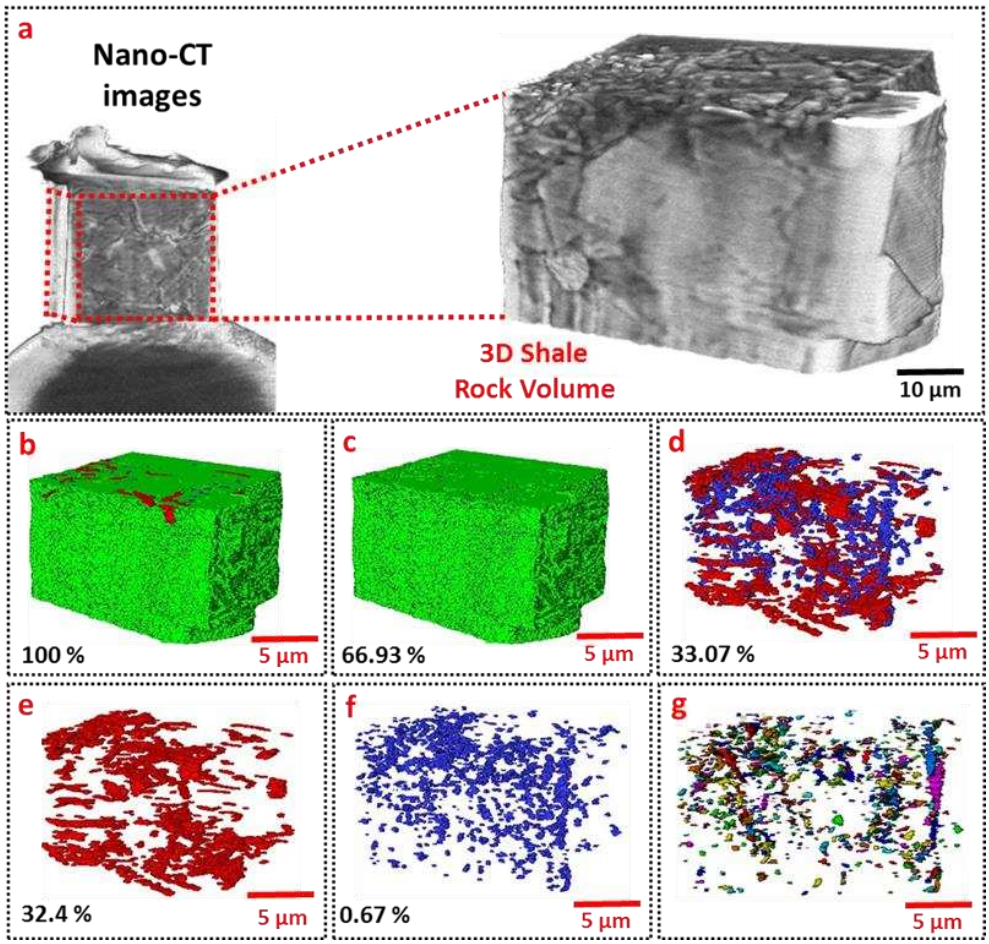

Figure 3. An overview of shale sample from Bowland gas shale that have been measured by X-ray nano-tomography (Nano-CT) (a) Raw 3D image with 25 μm^3 length cubic used in this study, (b) 3D image volume which is representative all phases within sample. By fixed thresholds values based on the greyscale on 3D image we can see (c) solid minerals (d) mixed kerogen and pores (e) the 3D of kerogen network presented in red, and (f) 3D of pores shown in blue. (g) The 3D image of pores where the colours indicate clusters of connected pores.

Table 2. Summary of the 3D imaging data for sample MD-2.7km from different techniques.

Method (Location)	Imaged size (µm³)	Voxel size (nm³)	Measured Porosity (%)	Measured Kerogen (%)	Calculated Permeability (nD)	Reference
FIB-SEM (A)	23×17×30	14×24×20	0.10 ± 0.01	34.8 ±1.74	13.85 ± 3.45	[17]
FIB-SEM (B)	34×25×40	27×34×50	0.52 ± 0.05	38.2 ±1.91	4.16 ± 1.04	
FIB-SEM (C)	28×22×40	21×26×50	0.94 ± 0.09	41.4 ±2.07	150 ± 37.5	
µ-CT	500×500×500	930×930×930	0.06 ±0.008	44.5 ±2.22	2.98 ± 0.745	
Nano-CT	25×25×25	64×64×64	0.67 ± 0.03	32.4 ±1.45	2.61 ± 0.42	This study

3.3 Pore volume distribution

Pore volumes were obtained using 3D image analysis of the nano-CT dataset at nanometric scale (i.e., with no smoothing). Figure 4 presents the distribution of the relative frequency of the number of pores as a function of their individual pore volume. The range of this distribution (0.02 µm³ and 0.35 µm³) reflects the range of scales over which the nano-CT provides data on pore volumes (the lower value represents the linear resolution of the technique, i.e., about 64 nm).

Figure 4 shows that there are a large number of pores with the smallest pore volumes, increasing to an unresolved peak at the lower limit of the technique. This suggests strongly that there is a large population of pores with smaller dimensions than the nano-CT technique can resolve. This is in agreement with our earlier FIB-SEM measurements [17] on the same rock sample. The FIB-SEM measurements have shown that there is a population of smaller pores, with volumes ranging between 3.6×10^{-5} µm³ to about 0.02 µm³ . It is these ultra-small pores which are likely to provide the connectivity required to allow gas to flow through shales, and whose small dimensions account for the low permeabilities of shale. These results are in agreement with the observation that pores lower than 10 nm are locally connected and can support diffusive or transitional gas transport [27]. Consequently, results from both nano-CT and FIB-SEM recognise the presence of a population of nanometric scale pores, but the nano-CT technique can only resolve the larger of these pores.

It should be noted that the small pores recognised by Javadpour et al. [17] and by ourselves using FIB-SEM [27] and now by nano-CT in this work represent a small proportion of the overall porosity of the rock despite their large number and irrespective of the possibility that they most likely control the transport properties of the rock.

Figure 4 also shows the same data but on a dual-logarithmic axes showing a negative power-law behaviour, which can be described by the equation $y=0.00347x^{-1.615}$ (R^2 =0.876). This observation suggests strongly that a large number of pores smaller than the resolution of the nano-CT technique is likely to be present in the sample. The distribution of pores as a function of pore volume has a fractal dimension $\mathcal{D}$ = 1.385.

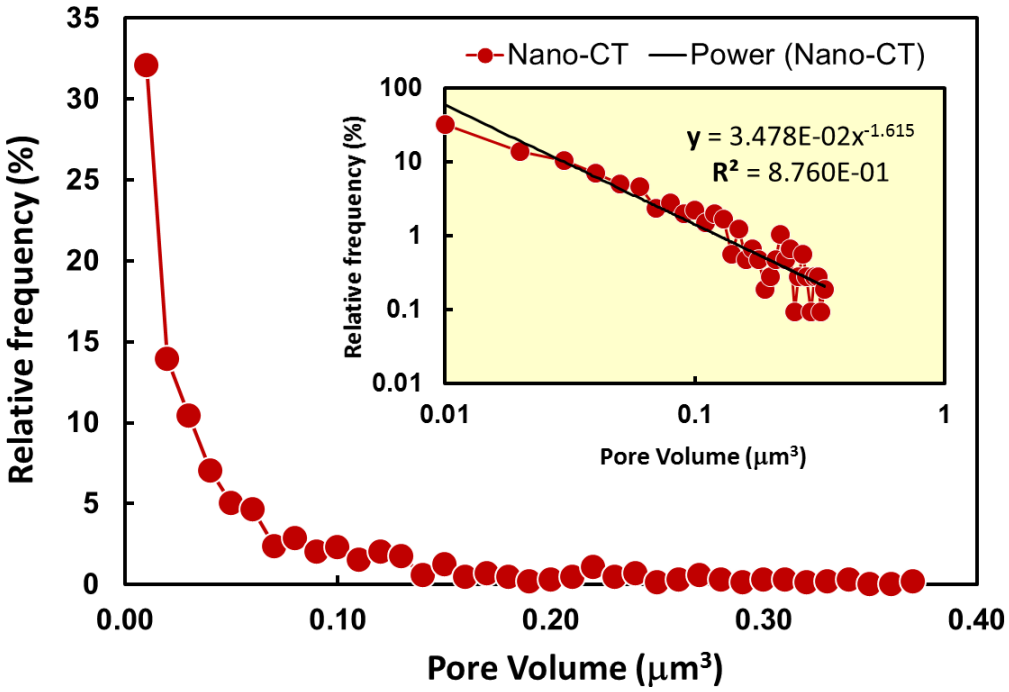

Figure 4. The distribution of the relative frequency of the number of pores as a function of their individual pore volume on a linear scale (inset: the same data on a dual-logarithmic scale).

3.4 Pore size distribution

The 3D imaging dataset from the nano-CT technique was also used to calculate the distribution of the relative frequency of the number of pores as a function of their individual pore size using the method in [17, 23]. These data have been compared to independent measurements of the relative frequency of the number of pores as a function of their individual pore size obtained using nitrogen adsorption and MIP for the same shale sample.

Figure 5 shows a comparison of the relative volume of pores as a function of their individual pore diameter as measured by nano-CT and MIP techniques. The MIP data provides a smaller range of pore sizes, from 3 to 2000 nm with a peak at about 9.2 nm, whereas the nano-CT measurement provides higher range of pore sizes, ranging between 100 nm to 5000 nm, with a peak at about 800 nm. Since the measurements were made on the same sample, the difference must be systematically linked to the techniques that were used to make the measurements. We could attribute the observed difference to an effect of having different scales for which each of the techniques is sensitive, because the two techniques do not completely overlap. The other possibility is that the MIP technique is measuring a population of pores which is compressed by the high mercury pressures needed to intrude mercury into the small pore spaces. Such an effect would be more likely to occur in relatively plastic shales with small pores, which is the case for our samples. The question remains, however, whether this effect could account for the two order of magnitude change that would be needed to produce the data observed in Figure 5.

Consequently, it would be reasonable to infer that the two different methods are measuring two different populations of pores present at different scales. This is because each technique has its own limitations in terms of sample size and resolution which has an impact on detecting pores within the sample [23], for example the lower pore size 3 nm can be detected by MIP and larger pores then 300 nm are shown by nano-CT.

Pore size and volume distributions less than 3 nm can be obtained by applying the BJH method to nitrogen absorption data (Figure 6). This technique measures the amount of gas molecules absorbed to (and subsequently desorbed from) the internal surfaces of pores as a function of applied gas pressure [28]. In this work the volume of the gas absorbed (and subsequently desorbed) has a range of 0.85-8.30 cm^3/g, with corresponding relative pressure (P/P^o) ranging between 0.07-0.9, respectively (Figure 6a), with a transform point of surface area equal to 0.2 (Figure 6b). The pore size distribution as a function of pore diameter, calculated using the BJH method is shown as Figure 6c, indicating progressively larger pore volumes occurring in the form of smaller pores. This is similar behaviour to what was observed for the nano-CT data in the inset of Figure 4. However, the data are not directly comparable since Figure 4 counts fractional pore numbers, while Figure 6c counts pore volume. Figure 6d provides the pore internal area distribution as a function of pore diameter.

Both Figure 6c and Figure 6d indicate the presence of significant pore volume and internal pore area for pores of the diameter of about 200 nm. This is consistent with the nano-CT data shown and discussed previously (red data in Figure 5). The nano-CT data show pores existing in the range 200-1200 nm (Figure 5). These cannot be observed in the nitrogen adsorption data due to limitations in the range of the nitrogen adsorption measurement. The gradual increase in both pore volume (Figure 6c) and pore area (Figure 6d) which occurs as the pore diameter progressively decreases below 800 nm is consistent with the FIB-SEM data (green data in Figure 5), where the relatively constant fraction of porosity observed by FIB-SEM between 100 nm and 10 nm corresponds to the straight line increase in the nitrogen adsorption data, and the more erratic changes in both the pore volume and pore area data between 10 nm and 2 nm may be associated with the peak in FIB-SEM fractional pore volume appearing in Figure 5.

According to the De Boer's classification [29], the pore shapes in this current shale sample are inferred to be penny-shaped (oblate), or to have a very small aspect ratio (i.e., small thickness relative to length). These observations are in broad agreement with analysis of the FIB-SEM data in our previous work [17] as well as the analysis of the nano-CT data in this work, as discussed below.

Table 3. Summary of petrophysical properties of gas shale rock sample in this paper from mercury injection porosimetry (MIP) and nitrogen adsorption (BET) techniques.

Sample	BET Surface area (m^2/g)	Single point of surface area (m^2/g)	Single point of pore volume (cm^3/g)	BET Porosity (%)	MIP Porosity (%)	Calculated Permeability from BET ($\times 10^{-4}$ nD)	Calculated Permeability from MIP (nD)
MD-2.7km	2.37	2.239	0.008488	0.0235± 0.003	0.6± 0.07	5.07± 0.02	2.65± 0.45

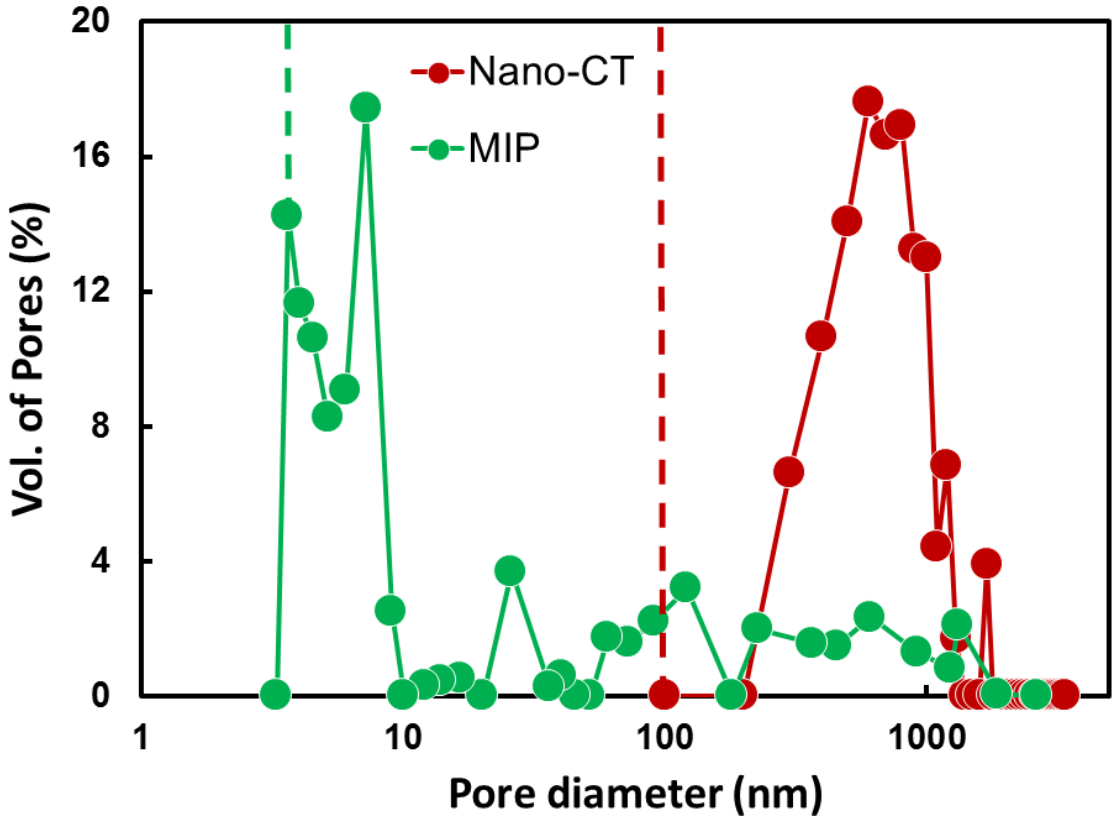

Figure 5. The pore size distribution estimated using two different measurements, Nano-CT (red) and MIP (green), made on the same shale sample. The dashed lines also present the lower limit of the native resolution for each method.

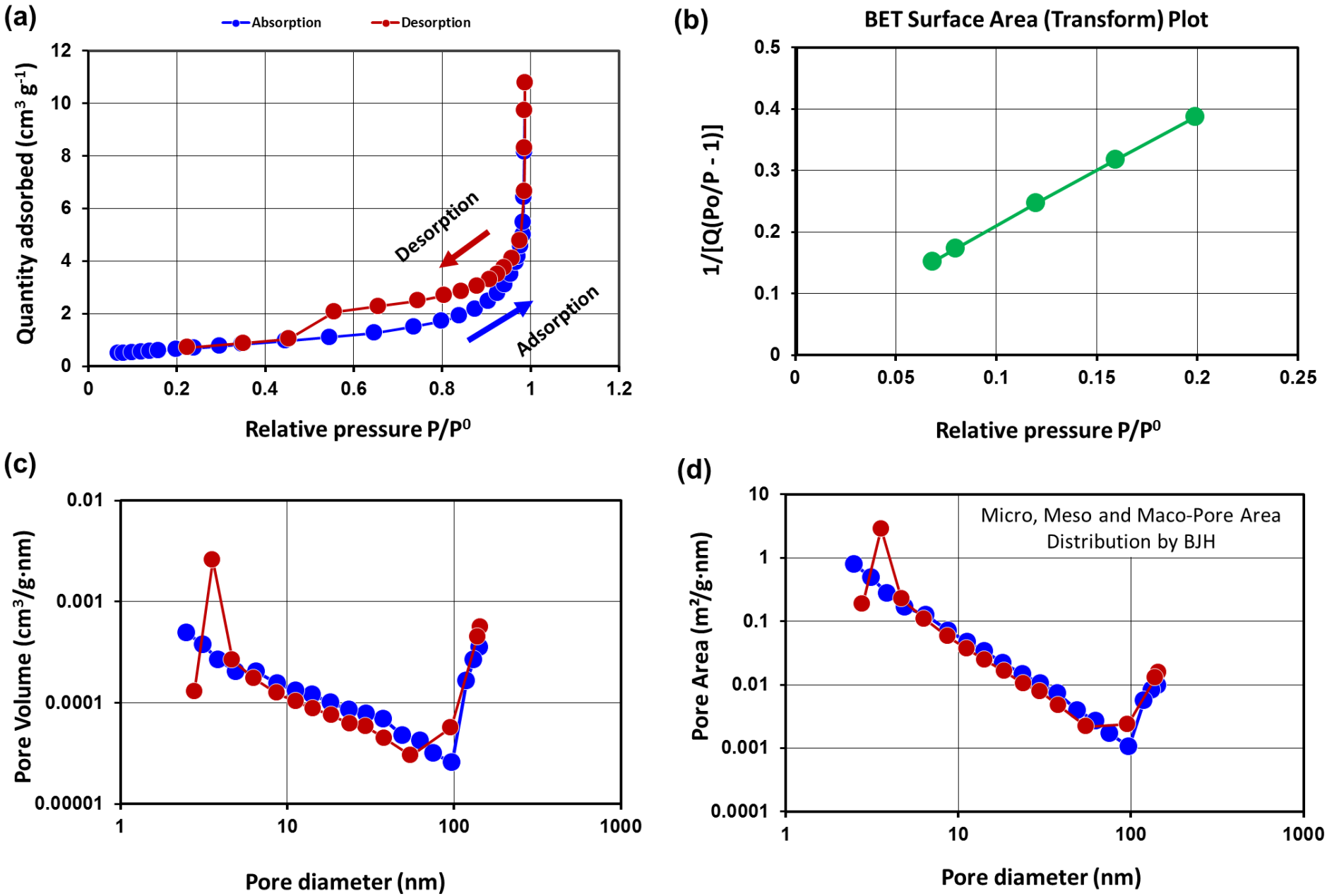
(a)
Absorption
Desorption
Quantity adsorbed (cm3 g-1)
Desorption
Adsorption
Relative pressure P/P0
(b)
BET Surface Area (Transform) Plot
1/[Q(Po/P - 1)]
Relative pressure P/P0
(c)
Pore Volume (cm3/g·nm)
Pore diameter (nm)
(d)
Micro, Meso and Maco-Pore Area Distribution by BJH
Pore Area (m2/g·nm)
Pore diameter (nm)

Figure 6. The pore size distribution calculated using nitrogen adsorption technique, (a) nitrogen N_2 adsorption measurement, the volume of the gas absorbed on the surface of pores per mass of sample at relative nitrogen pressures (P/P^o), (b) the BET surface area transform as a function of relative pressure (P/P^o), (c) the BJH pore size distribution as a function of pore diameter, and (d) the BJH pore area distribution as a function of pore diameter.

3.5 Pore aspect ratio distributions

The shape of pores can be extremely complex. However, it is often convenient to represent them as approximating to an ellipsoid, with orthogonal Cartesian semi-axes a, b and c. The shapes of individual pores can then be quantified in terms of aspect ratios, which are the ratios of any two of these semi-axes. The most commonly encountered aspect ratio is the ratio of the largest semi-axis to the smallest, such as the length of a crack to its aperture [17]. The entire spectrum of ellipsoidal shapes may be described by any two aspect ratios, from the needle-like prolate ellipsoids to the flat penny-shaped oblate ellipsoids.

In this paper we have followed a similar approach as in [17] by using the two pore aspect ratios $\gamma_1 = c/b$ and $\gamma_2 = a/c$, where c is defined as length of the smallest semi-axis, b is defined as length of the largest semi-axis and a is consequently the intermediate semi-axis.

Shales contain a significant amount of platy minerals which often form layers. Consequently, it is expected that most pores will exhibit a flat penny-shape. These oblate ellipsoids have $\gamma_1 << 1$ and $\gamma_2 > 1$ according to our definitions. The other main type of ellipsoid is pin-shaped or prolate, which have $\gamma_1 << 1$ and $\gamma_2 \approx 1$. Spherical or equant ellipsoids have $\gamma_1 \approx 1$ and $\gamma_2 \approx 1$.

We have calculated the γ_1 and γ_2 aspect ratios for each pore from the nano-CT 3D image data using Aviso. Figure 7 shows the percentage pore number and percentage pore volume distributions as a function of each aspect ratio, γ_1 (Figure 7a) and γ_2 (Figure 7b). Both parts of the need to be analysed together in order to fully understand the shape of the imaged pores.

First taking the distributions counted by pore number (blue data), Figure 7a shows that γ_1 varies from 0.065 to 0.8, representing pores which vary from those which are over 15 times longer than their smallest dimension to those which are near spherical (the longest dimension is only 1.25 times the smallest dimension and the intermediate dimension must be between the two extremes). Within this wide range of pore shapes there is a pronounced peak where over 36.47±0.05% of the pores have γ_1=0.1667±0.033, representing pores which are 6 times as longer than their smallest dimension. Contemporaneously, Figure 7b shows that γ_2 varies from 1.1 to 1.9, indicating that some pores are prolate ($\gamma_2 \rightarrow 1$) while others have a semi-axes up to almost twice the minimum dimension, indicating oblate or penny-shaped pores (i.e., $\gamma_2 > 1$). Once again, there is a peak in the distribution which represents about 34.57±0.05% of the number of pores at γ_2=1.457±0.0285. This data, when analysed in γ_1-γ_2 pairs shows that there is a significant well-defined sub-population of pores representing about 35% of the total pore number

which have a long axis about 6 times the short semi-axis, and an intermediate semi-axis about 1.457 times the short semi-axis.

It is interesting to note that the two distributions of the pore aspect (number and volume of pores) in both γ_1 and γ_2 are significantly different. As an example, let us take the same value of the γ_1 aspect ratio (say, 0.1667) in Figure 7a. γ_1 = 0.1667 represents about 17.11% of pore volume but 36.47% of the pores, which is suggests that the sub-population of pores discussed in the paragraph above, may stand out when the number of pores is counted (i.e., they are numerous) but do not stand out when counted by volume. One can, therefore, infer that these pores are relatively small because their numerousness does not particularly contribute to the overall pore volume.

Turning to the distributions counted by pore volume (red data), Figure 7a shows that γ_1 varies from 0.065 to 0.8. This is the same range as in the pore number distribution, and implies the same variation in pores from those which are over 15 times longer than their smallest dimension to those which are near spherical. However, there are no sharp peaks in the distribution. Instead, there is a broad peak at γ_1=0.30±0.167, amounting to just over 10% of the total pore volume and indicating that the longest dimension is only 3.33 times the smallest dimension. Figure 7b also shows that the distribution of γ_2 according to pore volume also varies within the same range as when counted by pore number (1.1 to 1.9). There is a relict of the peak in the distribution at about γ_2=1.457±0.0285, but this is swamped by larger values of γ_2<1.27. In other words, when counted by pore volume, pores for which $\gamma_2 \rightarrow 1$ (i.e., more prolate) are more dominant.

The distinction between oblate and prolate pores is important because each of these geometrical styles of pore will interact in a different fashion and lead to more or less connectivity for fluid transport.

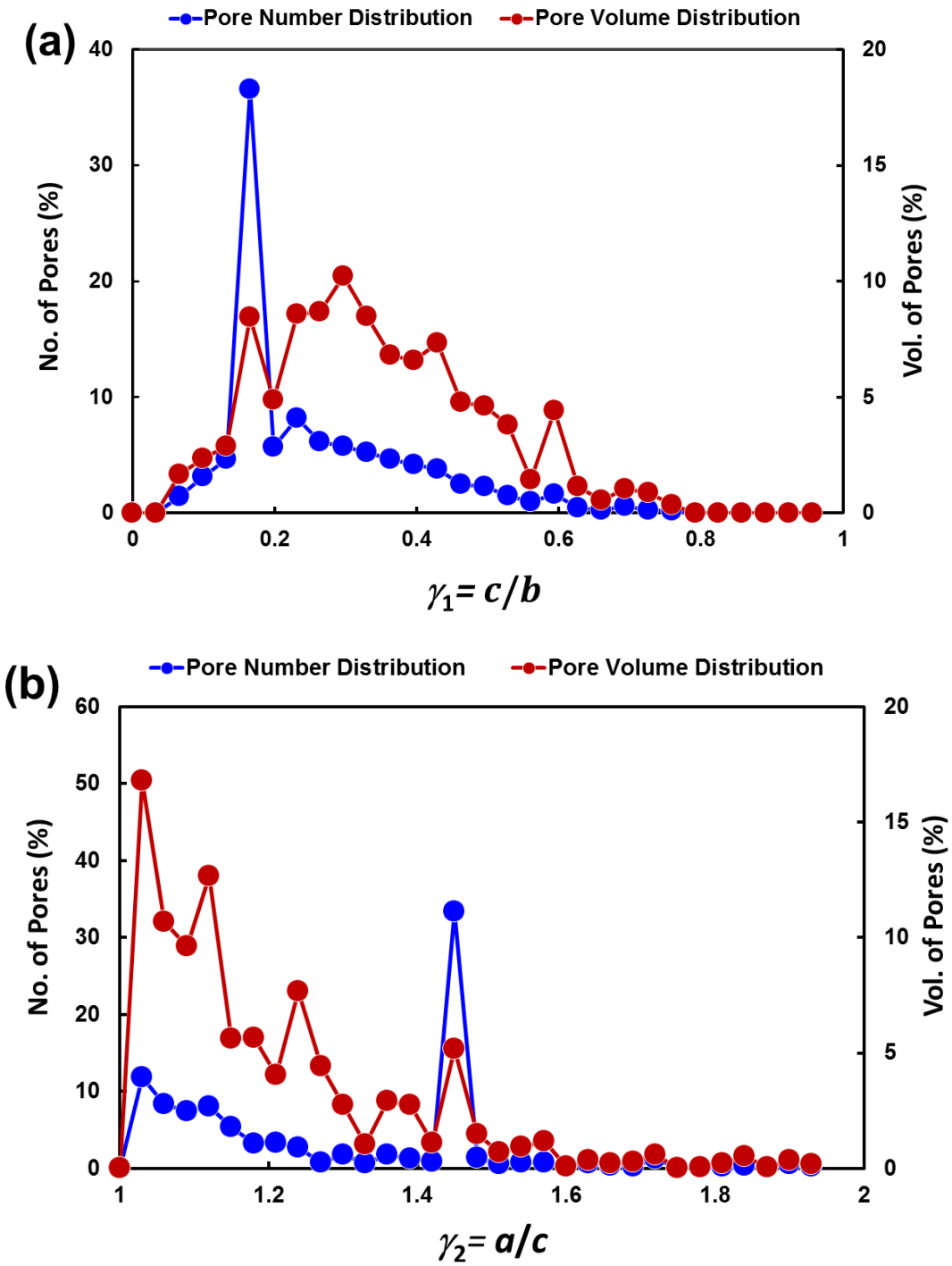

Figure 7. The pore number (blue) and pore volume (red) distributions of (a) γ_1, and (b) γ_2, calculated using Aviso 3D image analysis from 3D data obtained from applying the nano-CT imaging method to the MD-2.7 km gas shale sample.

3.6 Pore surface area to volume ratio

The pore surface area to volume ratio (ξ) is another important parameter for describing the shape of the pore within shale reservoir [17, 19, 23]. This ratio is very significant particularly in shale because large surface areas help the gas move more easily from the rock matrix

and from kerogen into the pores, which is a pre-requisite to hydraulic fracturing because gas must be able to transfer into the existing small pore spaces before stimulation can improve the connectivity of the small pore spaces sufficiently for gas to be produced. A high surface area ensures that the diffusion process is more efficient, not only ensuring a good initial charge of gas in the micro-pores of the shale, but also allowing those pores to be recharged quickly once initial production has removed the initially accumulated gas.

The ratio of the surface area to volume can be obtained analytically if it is assumed that all pores can be represented approximately by an ellipsoid shape [30], as described earlier. In this study, we have assumed that the oblate spheroids have semi-axis sizes according to $a \approx b > c$, i.e., spheres squashed in the c-direction, and approximating to penny-shaped cracks or pores. By comparison, prolate spheroids have semi-axis sizes conforming to $b > c \approx a$, i.e., spheres stretched in the b-direction, and approximating to needles. The volume for two types of spheroid can be determined using

$$V = \frac{4}{3}\pi abc. \quad \textbf{(1)}$$

If we assume that $a=b$ and that the shape of the ellipsoid is defined by the relative size of c with respect to ($a=b$), the surface areas of the two different types of spheroidal pore are given by

$$S_{oblate} = 2\pi a^2 \left(1 + \frac{c^2}{ea^2} \tanh^{-1} e\right), \text{ where } e^2 = 1 - \frac{c^2}{a^2}, \text{ if } a < c \quad \textbf{(2)}$$

$$S_{prolate} = 2\pi a^2 \left(1 + \frac{c}{ae} \sin^{-1} e\right), \text{ where } e^2 = 1 - \frac{a^2}{c^2}, \text{ if } a > c \quad \textbf{(3)}$$

In each case the term in brackets tends to 2 as c tends to a, the surface areas of the two types of spheroid are the same and are given by the surface area of a sphere of radius a

$$S_{oblate} = S_{prolate} = 4\pi a^2 \quad \textbf{(4)}$$

The surface area to volume ratio for each type of pore is then

$$\xi_{oblate} = \frac{3a}{2bc}\left(1 + \frac{c^2}{ea^2} \tanh^{-1} e\right), \text{ if } a < c, \text{ and} \quad \textbf{(5)}$$

$$\xi_{prolate} = \frac{3a}{2bc}\left(1 + \frac{c}{ae} \sin^{-1} e\right), \text{ if } a > c \quad \textbf{(6)}$$

With the value for a sphere ($a=b=c$) being $\xi_{sphere} = \frac{3}{a}$.

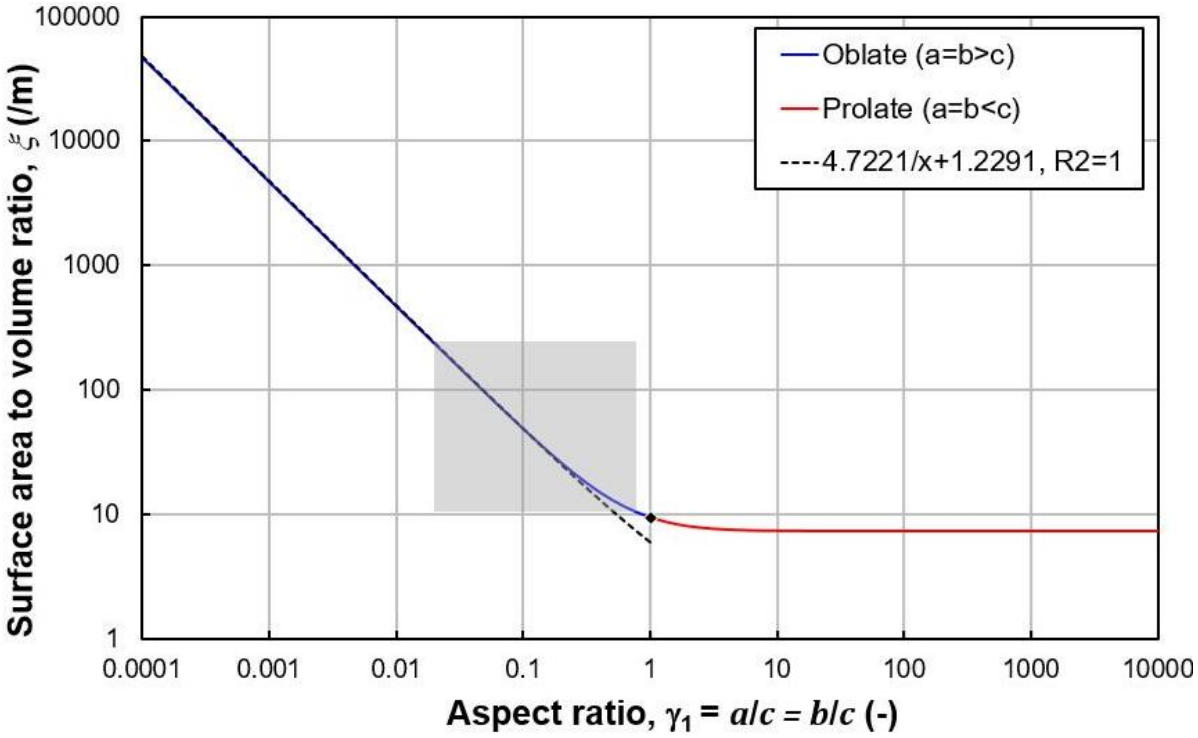

Figure 8. The surface area to volume ratio as a function of aspect ratio $\gamma_1=a/c$ for oblate spheroidal pores (γ_1>1) shown in blue, spherical pores (γ_1=1) shown by the symbol, and prolate spheroidal pores (γ_1<1), assuming that a=b. The grey box shows the range of values of γ_1 measured and represented in Figure 7a.

Figure 8 shows how the surface area to volume ratio depends on the γ_1 pore aspect ratio for both oblate and prolate pore shapes. The oblate pores (blue line) have significantly higher values of surface area to pore volume ratio than prolate pores (red line). The surface area to pore volume ratio of the oblate pores increases strongly as the aspect ratio increases, becoming asymptotic to $\xi = \frac{4.7122}{\gamma_1} + 1.2291$ with an R^2=1 for γ_1<0.2. The grey box in Figure 8 shows the range of γ_1 values measured in this work (see Figure 7a) indicating that these oblate pores would be expected to have surface area to volume ratios varying between 10.26 and 240 /m. We do not measure values in this range. The reason is that the simple surface area to volume ratio is scale dependent and the calculations that are carried out in Figure 8 are for a native scale of a=1 m. In order to overcome this problem a scale invariant surface area to volume ratio has been proposed [23].

Figure 9 shows the distributions of number of pores (blue data) and volume of pores (red data), both expressed as a percentage, as a function of the scale-invariant surface area to volume ratio, σ [23] for the nano-CT data presented in this paper. The mathematical definition of the scale-invariant surface area to volume ratio is such that only positive values greater than 3 are possible, representing a spherical pore. In our data the minimum value of σ was just greater than 3, while the maximum was about 13.

Figure 9 shows a uniform pore number distribution with a pronounced peak at about σ=3.5±0.5, which indicates that there is a large number of pores which are equant

(approximately spherical). However, the equivalent peak is much reduced in the pore volume distribution. We may infer, therefore, that the large number of equant pores are all very small. Indeed their apparent equant shape may be due to the fact that these are the single voxel pores that exist at the limits of the nano-CT resolution, and can consequently be considered to be artefacts of measurement. Figure 9 shows that pores with a broad range of σ values exist in the sample, some of which have very high values, representing pores which are extremely effective at degassing.

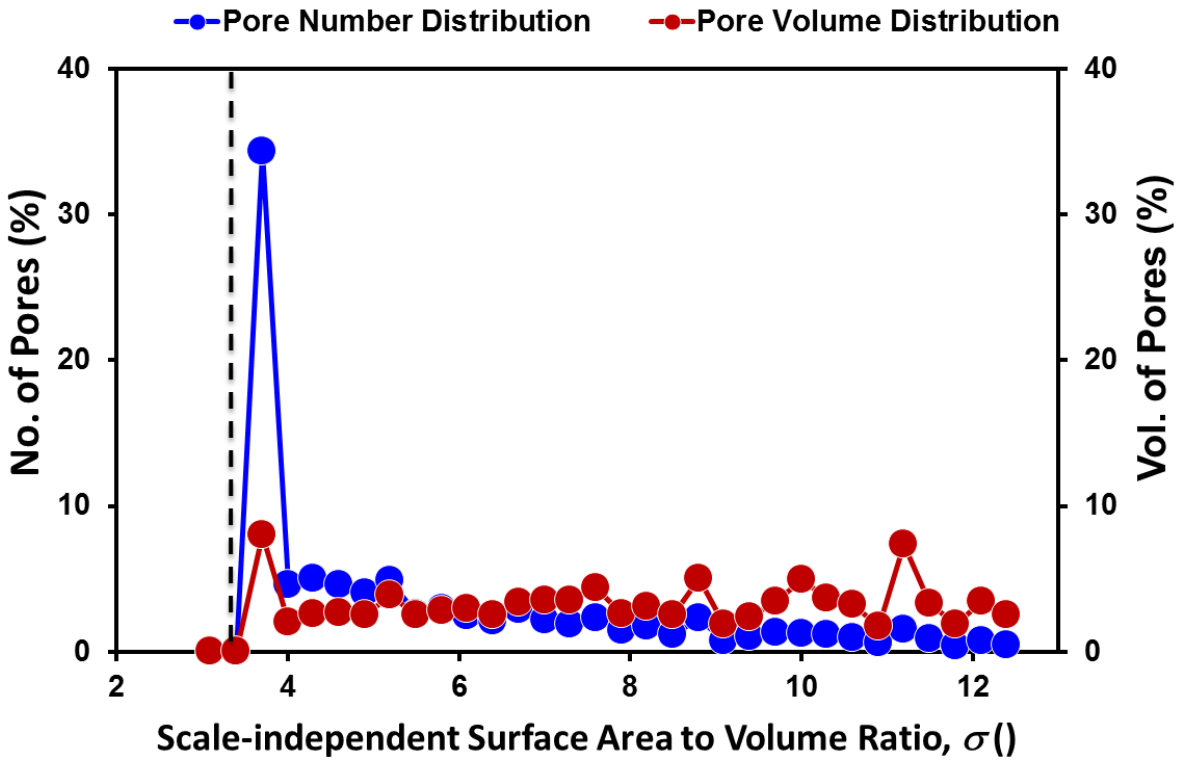

Figure 9. The pore number (blue) and pore volume (red) distributions of the scale invariant surface area to volume ratio σ, calculated using Aviso 3D image analysis from 3D data obtained from applying the nano-CT imaging method to the MD-2.7 km gas shale sample.

4. Permeability prediction

Permeability is a crucial parameter for assessing shale gas formations because it governs the ease of access to the hydrocarbon within the shale reservoir. However, it is extremely difficult to obtain directly especially in shale materials due to their highly heterogeneous microstructure as well as extremely small size of the pores.

There are very many ways to predict permeability, many of which are empirical. Here we restrict ourselves to those methods which do not need calibration to an empirical data set and for which we hold sufficient experimental data (imaging, nitrogen adsorption and MIP).

4.1 Nano-CT/Kozeny-Carman Permeability

In this study, we have used the Kozeny-Carman equation [31, 32] for predicting the permeability within the shale rock. This estimation is based on the specific surface area and porosity. This Kozeny–Carman equation is [33]:

$$k = \Psi^2 \frac{\phi^3 D_p^2}{180\,(1-\phi)^2}, \quad \textbf{(7)}$$

Where ϕ is porosity, D_p is the characteristic diameter of pores and Ψ is the sphericity of the pore. The sphericity is a measure of the geometrical shape of the pore in three-dimensions (i.e., how oblate or prolate). It was not determined in this study directly, but estimated based on the volume and surface area of the pore using [34]

$$\Psi = \frac{\pi^{1/3}\,(6V_p)^{2/3}}{S_p}, \quad \textbf{(8)}$$

Where V_p is the total volume of the pores and S_p is the total pore surface area.

The permeability for the MD-2.7 sample estimated by this method was found to be 2.61±0.42 nD for Nano-CT (Table 2).

4.2 MIP/RGPZ Permeability

The permeability can be estimated from MIP data by using the RGPZ model [35]. This model is derived analytically and does not need calibration. The RGPZ takes the heterogeneity of rock into consideration by using the electrical cementation exponent to represent the degree to which pores through the rock are connected. The RGPZ model is given by

$$K_{RGPZ} = \frac{d_{grain}^2 \phi^{3m}}{4am^2}, \quad \textbf{(9)}$$

Where d_{grain} is that grain diameter which dominates the flow characteristics within the porous medium, and was estimated using [36]

$$d_{grain} = 1.6585 \sqrt[2]{\frac{am^2}{8\,\phi^{2m}}}\, d_{pore\ throat}, \quad \textbf{(10)}$$

Where $d_{pore\ throat}$ is the size of a pore and was measured directly from MIP, and m is the cementation exponent (dimensionless) from the generalized Archie's law [37, 38]. The value of m = 3 was assumed in this study. This value was selected since the cementation exponent for shales is known to vary between about 2.34 and 4.17 [39]. The symbol ϕ is the porosity (as a fraction), which is obtained from the image analysis of the nano-CT data, and a is constant that is thought to be close to 8/3 for porous granular media [40].

The estimated permeability for the present sample by this method was found to be 2.65±0.45 nD (Table 3).

4.3 Nitrogen adsorption (BET)/Kozeny-Carman Permeability

The Kozeny-Carman equation was also used in this approach to estimate permeability, using nitrogen adsorption data to provide the specific surface area of the sample [41] and the image analysis data to provide porosity. This equation is given as

$$k = \frac{C_{kc}\phi^3}{S^2(1-\phi)^2}\ , \qquad \textbf{(11)}$$

where S is specific surface area (m^2/g) from the BET analysis, ϕ is the fractional porosity presented in Table 3, and C_{kc} is the Kozeny-Carman constant (2.064×10^{-13} $m^6\ kg^{-2}$) [41] which includes tortuosity and a generalised factor to account for different pore shapes [41].

The value of the permeability estimated from this approach was 5.07×10^{-4}±0.02 nD (Table 3).

5. Discussion and interpretation

In this work, we have extended our previous work [17] to describe the full pore range in the Bowland shale reservoir by implementing three more techniques.

The nano-CT imaging data indicates that the majority of pores have a volume ranging from 0.01 μm^3 to 0.35 μm^3 (Figure 4). By comparison, the pore volumes from FIB-SEM and µ-CT analysis were measured in the range 10^{-5} μm^3 to 0.0036 μm^3 for FIB-SEM and 0.9 μm^3 to 31.5 μm^3 for µ-CT [17]. Taken together, these three datasets imply that shale contains pores with volumes which cover the entire 4-decade measured range, from as small as 0.0036 μm^3 to 31.5 μm^3. There is no substantial evidence that the three populations observed by each of the three imaging techniques is separate from the point of view of its geometry or the process that have formed them. Rather, they are samples from a wider single continuous population of pores that has been sampled by the measured volume and native resolution of each technique. The same observation has also been made for shale in the work of [28, 42, and 43].

The shape and alignment of pores both provide significant control over gas transport in gas shales because they control the connectedness of pores and the tortuosity of flow paths [30, 44]. Hence the geometrical and connectivity properties of pores has the potential to exert important control on rock transport properties, including the electrical and hydraulic properties of rocks [30]. The shape of pores, parametrised particularly by the scale-invariant surface area to volume ratio, controls the efficacy of gas diffusion from kerogen into pores as well as along kerogen surfaces.

In the Bowland Shale the pores (0.67±0.009% of the total rock volume, Figure 3f) are mostly associated with the kerogen (32.4±1.45% of the total rock volume, Figure 3e), occupying space between the kerogen and the matrix of the rock or entirely within the kerogen. For this sample the pores with an equivalent diameter of 100 nm or larger have not shown connectivity, which has also been noted in the work of [45]. This observation encourages the interpretation (or classification) that kerogen should be considered to be more of a pore-filling phase rather than a rock matrix phase. The association of pores with kerogen has a number of implications. First, the kerogen ensures that the pores have a low connectivity. Second that the pores are well-positioned to be charged with gas diffusing out of the kerogen. Third, the connectivity of kerogen becomes particularly significant due to the potential presence of other transport forms such as surface diffusion and gas transport through kerogen. This observation raises the possibility that gas transport in shale might be modelled assuming that the connectivity of the kerogen controls gas transport. This latter approach has already been followed [23], producing values (0.003-1.66 nD) from nano-CT and FIB-SEM studies of Swedish gas shales that are not only consistent with other methodologies (2.55 nD and 9.92 nD) but also similar to permeability measurements made in the laboratory on the same material (1.74±0.65 nD).

In this work permeability calculations were possible using three different approaches. The values obtained were small, but typical of gas shales [23, 45]. Specifically, permeabilities of 2.61±0.42 nD from the nano-CT data, 2.65±0.45 nD from MIP, and (5.07±0.02) $\times 10^{-4}$ nD from the nitrogen adsorption (BET) method. The first two of these values are consistent with calculations, simulations and measurements made on a gas sale from Sweden [23]. The values are also broadly in agreement with three FIB-SEM measurements and one micro-CT measurement (13.85±3.45 nD, 4.16±1.04 nD, 150±37.5 nD, 2.98±0.745 nD, respectively) made previously on the same sample and published in [17]. The values suggests that our sample has very low connectivity but is not atypical. The very low value obtained from the nitrogen adsorption data can be explained. The nitrogen adsorption technique works well when pores are open and connected. The gas shale measured in this work has few, low connectivity pores that are mostly filled with kerogen. The result is that nitrogen cannot effectively penetrate the rock and that the overall calculated permeability is significantly underestimated.

6. Conclusions

In this study, we have characterized the microstructure of shale reservoir rock at different scales using a variety of technologies including nano-scale X-Ray tomography (nano-CT) with 3D image analysis, nitrogen adsorption, and mercury injection porosimetry (MIP). These three techniques were all implemented on the same Bowland gas shale sample. Furthermore, these methods have been carried out on the same sample that had already been imaged and

quantified using micro-CT and FIB-SEM methodologies [17]. The result is an unusually rich dataset that covers 4 decades of scale from about 20 nm to 0.5 mm with adjunct nitrogen adsorption and MIP data.

The results show a complex pore micro-structure that varies significantly at different scales in the sample. Overall the sample shows a porosity of 0.67±0.009% from the nano-CT data, 0.0235±0.003% from nitrogen adsorption, and 0.60±0.07% from MIP, which compare with 0.10±0.01%, 0.52±0.05%, 0.94±0.09% from 3 FIB-SEM measurements and 0.06±0.008% from micro-CT measurements all made by ourselves previously on the same sample [17]. The data vary due to the different scales at which each technique interrogates the rock and whether the pores are openly accessible (especially in the case of the nitrogen adsorption value).

Likewise, the measured kerogen content of the rock varies. In this work the measured kerogen fraction is 32.4±1.45%, compared with 34.8±1.74%, 38.2±1.91%, 41.4±2.07%, and 44.5±2.22% for 3 FIB-SEM measurements and a micro-CT measurement done on the same sample and reported in [17].

The Bowland shale sample shows pores at all scales. The pore size imaged by nano-CT ranged between 100 nm to 5000 nm, while the corresponding ranges were between 3 and 2000 nm for MIP analysis and between 2 nm to 90 nm for N_2 adsorption. The associate measured pore volumes ranged from 0.01 μm^3 to 0.35 μm^3 from the nano-CT data presented in this work. However, we know that pore volumes as low 10^{-5} μm^3 have been measured for the same sample by FIB-SEM and as high as 31.5 μm^3 for the same sample by micro-CT [17].

The distribution of pore aspect ratio and scale-invariant pore surface area to volume ratio (σ) as well as the calculated permeability shows sample MD-2.7 to be a shale sample with a high shale gas potential. The aspect ratios indicate that most of the pores which contribute significantly to pore volume are oblate. In addition, the range scale-invariant pore surface area to volume ratio (σ) has been found to vary from 3 to 13 which also suggests that the pores imaged by the nano-CT method tend to be oblate. Oblate pores have greater potential for interacting with other pores compared to equant and needle-shaped prolate pores, as well optimising surface area for gas to desorb from the kerogen into the pores.

A number of permeability calculations have also been carried out, providing 2.61 nD from the nano-CT data, 2.65 nD from the MIP data, and 5.07×10^{-4} nD from the nitrogen adsorption (BET) method. With the expected exception of the methodology relying on nitrogen adsorption measurements, all permeabilities were in reasonable agreement with each other, the expectations for generic gas shales (i.e., tens of nD) and the measurements made previously [17] on the same sample using FIB-SEM and micro-CT imaging techniques.

This study has extended our knowledge to an enhanced understanding the internal microstructure of the Bowland shale reservoir within Lancashire, UK, as well as flow properties including pore and kerogen connectivity which are essential in transport in shale rock reservoirs. The multi-scale interpretations that are possible when combining the results of this study with studies on the same and related samples [17, 19, 23] lead to a better understanding the pore system, network of kerogen and mineral in shales across 4 orders of magnitude of scale.

The results of this type of multi-scale imaging can be useful not only for shale gas but also for other many applications such as the study of reservoirs and cap-rocks for carbon sequestration, geothermal reservoirs and potential sites for the long-term disposal of radioactive material.

7. Acknowledgments

The authors would like to thank the support of the Royce Ph.D. Equipment Access Scheme (EPSRC Grant Number EP/20/008), and to Leeds University Electron Microscopy and Spectroscopy Centre (LEMAS) for their technical support.

References

1. Du, H., Radonjic, M. and Chen, Y., 2020. Microstructure and micro-geomechanics evaluation of Pottsville and Marcellus shales. Journal of Petroleum Science and Engineering, 195, p.107876.
2. Peng, S., Hu, Q., Dultz, S. and Zhang, M., 2012. Using X-ray computed tomography in pore structure characterization for a Berea sandstone: Resolution effect. Journal of Hydrology, 472, pp. 254-261.
3. Lazar, O.R., Bohacs, K.M., Macquaker, J.H., Schieber, J. and Demko, T.M., 2015. Capturing Key Attributes of Fine-Grained Sedimentary Rocks In Outcrops, Cores, and Thin Sections: Nomenclature and Description Guidelines. Journal of Sedimentary Research, 85(3), pp. 230-246.
4. Chalmers, G.R., Bustin, R.M. and Power, I.M., 2012. Characterization of gas shale pore systems by porosimetry, pycnometry, surface area, and field emission scanning electron microscopy/transmission electron microscopy image analyses: Examples from the Barnett, Woodford, Haynesville, Marcellus, and Doig units Characterization of Gas Shale Pore Systems. AAPG Bulletin, 96(6), pp. 1099-1119.
5. Klaver, J., Desbois, G., Littke, R. and Urai, J.L., 2015. BIB-SEM characterization of pore space morphology and distribution in postmature to overmature samples from the Haynesville and Bossier Shales. Marine and Petroleum Geology, 59, pp. 451-466.
6. McKernan, R.E., Rutter, E.H., Mecklenburgh, J., Taylor, K.G. and Covey-Crump, S.J., 2014, February. Influence of effective pressure on mudstone matrix permeability: implications for shale gas production. In SPE/EAGE European Unconventional Resources Conference and Exhibition (Vol. 2014, No. 1, pp. 1-13). European Association of Geoscientists & Engineers.
7. Ougier-Simonin, A., Renard, F., Boehm, C. and Vidal-Gilbert, S., 2016. Microfracturing and microporosity in shales. Earth-Science Reviews, 162, pp. 198-226.
8. Ambrose, R.J., Hartman, R.C., Diaz-Campos, M., Akkutlu, I.Y. and Sondergeld, C.H., 2010. New pore-scale considerations for shale gas-in-place calculations. SPE-131772, paper presented at the Unconventional Gas Conference, SPE, Pittsburgh, PA, February 23-25.
9. Sondergeld, C.H., Ambrose, R.J., Rai, C.S. and Moncrieff, J., 2010. Micro-structural studies of gas shales. In SPE Unconventional Gas Conference. Society of Petroleum Engineers.
10. Clarkson, C.R., Solano, N., Bustin, R.M., Bustin, A.M.M., Chalmers, G.R.L., He, L., Melnichenko, Y.B., Radliński, A.P. and Blach, T.P., 2013. Pore structure characterization of North American shale gas reservoirs using USANS/SANS, gas adsorption, and mercury intrusion. Fuel, 103, pp. 606-616.

11. Guise, P., Grattoni, C. A., Allshorn, S. L., Fisher, Q. J and Schiffer, A., 2018. Stress Sensitivity of Mercury-Injection Measurements. Petrophysics, 59, 25-34.
12. Clarkson, C.R., Jensen, J.L. and Blasingame, T., 2011. Reservoir engineering for unconventional reservoirs: what do we have to consider. In North American Unconventional Gas Conference and Exhibition. Society of Petroleum Engineers.
13. Yuan, Y. & Rezaee, R., 2019. Comparative Porosity and Pore Structure Assessment in Shales: Measurement Techniques, Influencing Factors and Implications for Reservoir Characterization. Energies, 12.
14. Bustin, R.M., Bustin, A.M., Cui, A., Ross, D. and Pathi, V.M., 2008. Impact of shale properties on pore structure and storage characteristics. In SPE shale gas production conference. Society of Petroleum Engineers.
15. Guo, B., Ma, L. and Tchelepi, H.A., 2018. Image-based micro-continuum model for gas flow in organic-rich shale rock. Advances in Water Resources, 122, pp. 70-84.
16. Ma, L., Dowey, P., Fauchille, A.L., Taylor, K. and Lee, P., 2017. Correlative multi-scale 3D imaging of shales: An example from the Haynesville-Bossier Shale, southeast USA. EGUGA, p. 3809.
17. Garum, M., Glover, P.W., Lorinczi, P., Drummond-Brydson, R. and Hassanpour, A., 2020a. Micro-and Nano-Scale Pore Structure in Gas Shale Using Xμ-CT and FIB-SEM Techniques. Energy & Fuels, 34(10), pp. 12340-12353.
18. Curtis, M.E., Sondergeld, C.H., Ambrose, R.J. and Rai, C.S., 2012. Microstructural investigation of gas shales in two and three dimensions using nanometer-scale resolution imaging. Microstructure of Gas Shales. AAPG Bulletin, 96(4), pp. 665-677.
19. Garum, M., Glover, P., Lorinczi, P. and Hassanpour, A., 2020b. Ultrahigh resolution 3D imaging and characterisation of nanoscale pore structure in shales and its control on gas transport. In EGU General Assembly Conference Abstracts (p. 45).
20. Joyce, S., Hartley, L., Applegate, D., Hoek, J. and Jackson, P., 2014. Multi-scale groundwater flow modeling during temperate climate conditions for the safety assessment of the proposed high-level nuclear waste repository site at Forsmark, Sweden. Hydrogeology Journal, 22(6), pp. 1233-1249.
21. Lichtner, P.C. and Karra, S., 2014. Modeling multiscale-multiphase-multicomponent reactive flows in porous media: Application to CO2 sequestration and enhanced geothermal energy using PFLOTRAN. Computational Models for CO2 Geo-sequestration & Compressed Air Energy Storage, pp. 81-136.
22. Lu, X., Taiwo, O.O., Bertei, A., Li, T., Li, K., Brett, D.J. and Shearing, P.R., 2017. Multi-length scale tomography for the determination and optimization of the effective microstructural properties in novel hierarchical solid oxide fuel cell anodes. Journal of Power Sources, 367, pp. 177-186.
23. Garum, M., Glover, P.W., Lorinczi, P., Scott, G. and Hassanpour, A., 2020c. Ultrahigh-Resolution 3D Imaging for Quantifying the Pore Nanostructure of Shale and Predicting Gas Transport. Energy & Fuels.
24. Brunauer, S., Emmett, P.H. and Teller, E., 1938. Adsorption of gases in multimolecular layers. Journal of the American chemical society, 60(2), pp. 309-319.
25. Barrett, E.P., Joyner, L.G. and Halenda, P.P., 1951. The determination of pore volume and area distributions in porous substances. I. Computations from nitrogen isotherms. Journal of the American Chemical society, 73(1), pp. 373-380.
26. Bhargava, S., Awaja, F. and Subasinghe, N.D., 2005. Characterisation of some Australian oil shale using thermal, X-ray and IR techniques. Fuel, 84(6), pp. 707-715.

27. Javadpour, F., Fisher, D. and Unsworth, M., 2007. Nanoscale gas flow in shale gas sediments. Journal of Canadian Petroleum Technology, 46(10).
28. Sing, K., 2001. The use of nitrogen adsorption for the characterisation of porous materials. Colloids and Surfaces A: Physicochemical and Engineering Aspects 187, 3-9.
29. De Boer, J.H. and Lippens, B., 1964. Studies on pore systems in catalysts II. The shapes of pores in aluminium oxide systems. Journal of Catalysis, 3(1), pp. 38-43.
30. Glover P.W.J. 2009. What is the cementation exponent? A new interpretation: The Leading Edge, 556, 82-85.
31. Bear, J., 1988. Dynamics of fluids in porous media. Elsevier, New York.
32. Mostaghimi, P., Blunt, M.J. and Bijeljic, B., 2013. Computations of absolute permeability on micro-CT images. Mathematical Geosciences, 45(1), pp. 103-125.
33. Kozeny, J., 1927. Uber kapillare leitung des wassers in boden: Sitzungsberichte der Wissenscha ften, 136, 271–306.
34. Busch, A., Schweinar, K., Kampman, N., Coorn, A., Pipich, V., Feoktystov, A., Leu, L., Amann-Hildenbrand, A. and Bertier, P., 2017. Determining the porosity of mudrocks using methodological pluralism. Geological Society, London, Special Publications, 454(1), pp. 15-38.
35. Glover, P.W., Zadjali, I.I. and Frew, K.A., 2006. Permeability prediction from MICP and NMR data using an electrokinetic approach. Geophysics, 71(4), pp. F49-F60.
36. Glover, P.W. and Walker, E., 2009. Grain-size to effective pore-size transformation derived from electrokinetic theory. Geophysics, 74(1), pp. E17-E29
37. Glover, P.W.J., 2010. A generalized Archie's law for n phases. Geophysics, 75(6), pp. E247-E265.
38. Glover, P. W. J. Geophysical Properties of the Near Surface Earth: Electrical Properties. In Gerald Schubert (Editor-in-Chief) Treatise on Geophysics, 2nd ed.; Elsevier: Oxford, 2015; Vol. 11, pp 89– 137.
39. Revil, A. and Cathles Iii, L.M., 1999. Permeability of shaly sands. Water Resources Research, 35(3), pp. 651-662.
40. Rashid, F., Glover, P.W.J., Lorinczi, P., Collier, R. and Lawrence, J., 2015. Porosity and permeability of tight carbonate reservoir rocks in the north of Iraq. Journal of Petroleum Science and Engineering, 133, pp. 147-161.
41. Eseme, E., Krooss, B.M. and Littke, R., 2012. Evolution of petrophysical properties of oil shales during high-temperature compaction tests: Implications for petroleum expulsion. Marine and Petroleum Geology, 31(1), pp. 110-124.
42. Kuila, U. and Prasad, M., 2013. Specific surface area and pore-size distribution in clays and shales. Geophysical Prospecting, 61 (Rock Physics for Reservoir Exploration, Characterisation and Monitoring), pp. 341-362.
43. Ma, L., Slater, T., Dowey, P.J., Yue, S., Rutter, E.H., Taylor, K.G. and Lee, P.D., 2018. Hierarchical integration of porosity in shales. Scientific reports, 8(1), pp. 1-14.
44. Clennell, M. B. 1997. Tortuosity: a guide through the maze. Geological Society, London, Special Publications, 122, 299-344.
45. Ma, L., Taylor, K.G., Lee, P.D., Dobson, K.J., Dowey, P.J. and Courtois, L., 2016. Novel 3D centimetre-to nano-scale quantification of an organic-rich mudstone: The Carboniferous Bowland Shale, Northern England. Marine and Petroleum Geology, 72, pp. 193-205.